Multiwavelength Study of the X-ray Bright Supernova Remnant N300-S26 in NGC 300

Jacob Gross[1], Benjamin F. Williams[1], Thomas G. Pannuti[2], Breanna Binder[3], Kristen Garofali[4], Zachary G. Hanvey[2]

[1]Department of Astronomy, Box 351580, University of Washington, Seattle, WA 98195

[2]Space Science Center, Department of Earth and Space Sciences, 235 Martindale Drive, Morehead State University, Morehead, KY 40351

[3]Department of Physics and Astronomy, California State Polytechnic University, 3801 West Temple Ave, Pomona, CA 91768

[4]Department of Physics, 825 West Dickson Street, University of Arkansas, Fayetteville, AR 72701

ABSTRACT

We present a multiwavelength examination of the supernova remnant (SNR) S26 in the nearby galaxy NGC 300 using data from *Chandra X-ray Observatory*, *XMM-Newton X-ray Observatory*, *Hubble Space Telescope* (HST), the *Very Large Array*, and the *Australia Telescope Compact Array*. We simultaneously fit all of the available X-ray data with a thermal plasma model and find a temperature of 0.77 ± 0.13 keV with a hydrogen column density of $(9.7^{+6.4}_{-4.8}) \times 10^{20}$ cm^{-2}. HST imaging allows us to measure a semimajor axis of 0.78 ± 0.10 arcsec (7.5 ± 1.0 pc) and a semiminor axis of $0.69^{+0.14}_{-0.12}$ arcsec ($6.7^{+1.2}_{-1.4}$ pc). This precise size helps to constrain the age and velocity of the shock to be $(3.3^{+0.7}_{-0.6}) \times 10^3$ yr and 411^{+275}_{-122} km s^{-1}. We also fit photometry of the surrounding stars to infer the age and mass of the progenitor star to be 8 ± 1 Myr and 25^{+1}_{-5} M$_\odot$. Based on measured radio properties of the source and assuming equipartition, the estimated radio luminosity of $\sim 1.7 \times 10^{34}$ erg s^{-1} over the 10^8 to 10^{11} Hz frequency range results in a minimum magnetic field associated with this SNR of 0.067 mG and the minimum energy needed to power the observed synchrotron emission of 1.5×10^{49} erg. The size and temperature of N300-S26 appear to be similar to the Galactic SNR G311.5–0.3 except that G311.5–0.3 has a significantly lower X-ray luminosity, is older, and has a slower shock velocity.

Subject headings: Supernovae: individual (N300-S26), X-rays: individual (N300-S26), ISM: supernova remnants

1. Introduction

The energy output of supernova remnants (SNRs) shock and excite the interstellar medium (ISM), which makes them visible across the electromagnetic spectrum out to distances of megaparsecs. While the Milky Way SNR population is closest to us, many of its SNRs are difficult to observe due to interstellar absorption along Galactic lines of sight and uncertainties in distance measurements. Analyses of SNRs outside our Galaxy provide key comparisons to the Galactic sample that probe differences in the ISM and how it influences SNR's multiwavelength morphological luminosity evolution. Since the nearby galaxy population contains a wide range of ISM densities and metallicities, detailed multiwavelength measurements of the SNRs allow us to shed light on the effects of the environment on SNR properties.

There have been many SNR surveys of nearby galaxies including the Large Magellenic Cloud (LMC) (Desai et al. 2010; Seok et al. 2013; Bozzetto et al. 2017), M31 (Kong et al. 2003; Jennings et al. 2014; Lee & Lee 2014a), M33 (Long et al. 2010b; Jennings et al. 2014; Lee & Lee 2014b), and M83 (Blair et al. 2012; Long et al. 2014; Winkler et al. 2017). One such galaxy is NGC 300, a face-on spiral ScD galaxy at 2 Mpc (Dalcanton et al. 2009), which is the brightest of the five main spiral galaxies in the Sculptor Group (Rodríguez et al. 2016). The 46° inclination of NGC 300 (Freedman et al. 1992) as well as the Galactic latitude of −79.4 degrees (which places NGC 300 toward the southern Galactic pole; Dalcanton et al. (2009)) allows it to be observed easily due to reduced absorption effects from gas in the host galaxy as well as our Galaxy. There are many different surveys of NGC 300's SNR population including, but not limited to, optical (Dodorico et al. 1980; Blair & Long 1997; Millar et al. 2011), radio (Pannuti et al. 2000), and X-ray (Payne et al. 2004; Carpano et al. 2005). All of this data allows for a detailed measurement of the physical properties of SNRs in NGC 300.

Multiwavelength observations of SNRs provide details about the energetics and evolution associated with these sources. The X-ray, optical, and radio emission from SNRs probe the magnetic fields created by the source, the energy needed to drive synchrotron radiation, the temperature and column density of the surrounding gas, the physical size and velocity of the associated shock waves, and many other properties. These SNR properties should, in principle, be related to both the physical parameters of the progenitor star and those of the surrounding ISM.

We have observed a bright extragalactic SNR in NGC 300 denoted as N300-S26 (Dodorico et al. (1980); Blair & Long (1997); hereafter referred to as S26). Previous observations of S26 have included various radius measurements taken from multiple optical ground-based telescopes (1.7 arcsec which corresponds to 16.5 pc at the assumed distance to NGC 300; Dodorico et al. (1980); Blair & Long (1997)), Hα surface brightness (Blair & Long 1997), radio flux density (Pannuti et al. 2000; Payne et al. 2004), as well as a temperature from the *ROSAT* telescope (Read et al. 1997).

In this paper, we have observed S26 in the optical using *Hubble Space Telescopes* (*HST*), in the X-ray by *Chandra* and *XMM-Newton*, and in the radio using the *Very Large Array* (*VLA*) and *Australia Telescope Compact Array* (*ATCA*) from Pannuti et al. (2000) and Payne et al. (2004). We then compare S26 to other SNRs in the Galaxy, finding that S26 is most similar to G311.5–0.3, which has a temperature of $0.68^{+0.20}_{-0.24}$ keV and a radius of 9 pc. In section 2, we discuss the data sets used in our study and the methods utilized to extract information from the raw data. In section 3, we share our results from our data reductions. In section 4, we discuss the physical ramifications of our measurements. In section 5, we summarize our results.

Values derived in the radio sections are at the 90% confidence range. The values derived in the X-ray sections for the `tbabs*(pshock)` normalization tied model are at the

90% confidence range while the other models are at the 1σ limit.

2. Observations and Data Reduction

Our multiwavelength program makes use of data from the *HST* (optical), the *Chandra X-ray Observatory* (*Chandra*; X-ray), the *XMM-Newton X-ray Observatory* (*XMM-Newton*; X-ray), the *VLA* (radio), and the *ATCA* (radio) (radio data from Pannuti et al. (2000) and Payne et al. (2004)). We now discuss each of these in detail below.

2.1. Optical Data

We detected the optical shell of S26 with the Advanced Camera for Surveys on board the *HST* at 0:55:15.447, −37:44:39.10 (J2000). The data were obtained with the WFC detector using F814W and F606W filters on 2015 January 19. The F814W filter had a 966 s exposure and the F606W filter had a 850 s exposure. While the broadband SNR fluxes would not be useful for science, as they contain multiple emission lines and have a dense background of stars, the high-resolution imaging allowed us to measure a precise size for the optical shell. In addition, the field of resolved stars allowed us to perform crowded stellar field photometry on the stellar population local to the SNR, which provides constraints on the mass of the star that produced the SNR. We detail the analysis techniques we employed for each of these applications below.

2.1.1. Optical SNR Size Measurement

We used Deep Space 9 (DS9) version 7.2.1[1] to create an RGB-rendered image of the source using F606W for the green channel, F814W for the red channel, and an estimated blue channel of $2 \times$ F606W $-$ F814W (Figure 1). We then used ellipses to measure the size of the SNR to a significantly higher precision than previous studies due to the *HST*'s superior spatial resolution (see section 3.1 for details).

In order to corroborate the size measurement using ellipses, we used the DS9 tool `Projections` to create surface brightness functions along the semimajor and semiminor axes.

2.1.2. Resolved Stellar Photometry

We also measured resolved stellar photometry from the *HST* images in order to produce color-magnitude diagrams (CMDs) of the stellar populations surrounding the SNR using the VEGAMAG system. The photometry was performed using the automated point spread function (PSF) fitting pipeline from the Panchromatic Hubble Andromeda Treasury. The full details of how the pipeline works are given in Williams et al. (2014b), but briefly, the calibrated flat-fielded and CTE corrected (`flc`) *HST* images are masked and analyzed using a combination of the PyRAF routine `astrodrizzle` and the photometry package DOLPHOT, an updated version of HSTPHOT (Dolphin 2000). The analysis is performed on the full set of images simultaneously, where the locations of stars are found using the statistics of the full stack of images, and the photometry is performed through forcing PSF fitting at all of the star locations on all of the individual exposures. The resulting measurements are combined and culled based on signal to noise and measurement quality. We then perform a series of artificial star tests, whereby a star of known color
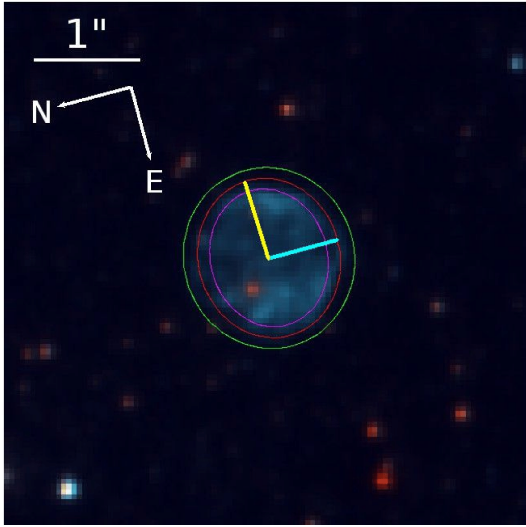
---

[1]http://ds9.si.edu/site/Home.html

Fig. 1.—:

Top: Optical image of S26 using F606W and F814W filters as well as an estimated blue channel using 2 × F606W - F814W. The semiminor axis is depicted with the blue line while the semimajor axis is depicted with the yellow line.

Middle: Semiminor measurement using Surface Brightness Function aligned with semiminor axis taken from the optical image.

Bottom: Semimajor measurement using Surface Brightness Function aligned with semimajor axis taken from the optical image.
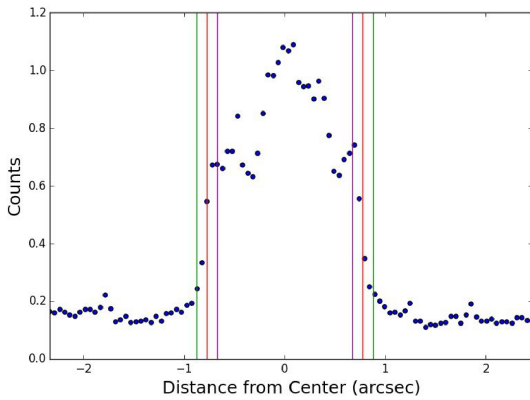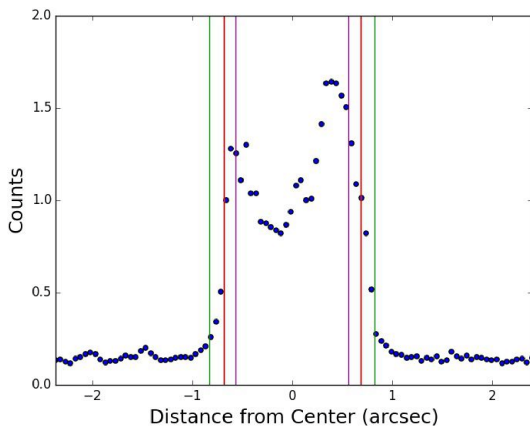
Green ellipse and vertical lines correspond to upper limit to fit. Red ellipse and vertical lines correspond to best-fit. Purple ellipse and vertical lines correspond to the lower limit to fit.

and magnitude is inserted into the images and the photometry routine is rerun to assess whether the star was recovered, and how the output magnitude compared to the input.

This exercise is repeated 10^5 times to build up statistics on completeness, photometric bias, and photometric error, as a function of color and magnitude. For example, the artificial stars showed that our completeness falls below 50% at F606W=27.9 and F814W=27.1, and the uncertainties at those magnitudes is $27.9^{+0.4}_{-0.2}$ and $27.1^{+0.3}_{-0.2}$ for F606W and F814W, respectively. The asymmetric uncertainties are due to the bias of faint stars being measured brighter than their true flux due to crowding effects.

2.2. X-Ray Data

The X-ray data used were three *Chandra* and six *XMM-Newton* observations. The information about each observation can be seen in Table 1. The SNR is near two other sources, as shown in Figure 2; however, it is separated enough from these (30.1 and 50.1 arcsec for the two objects) that we were able to mask them out as shown in the figure. We discuss the details of these observations below.

2.2.1. *Chandra Data*

We extracted the spectroscopic data using Ciao v.4.6.7[2] and CALDB v4.1[3]. Since the source was unresolved in X-rays, we adopted the point-source extraction method for the spectrum from the `specextract` command[4]. We have a total of three observations using the ACIS detector totaling an exposure of 191 ks (see Table 1). For this, we selected regions centered on S26, which enclosed the entire source within a circle of radius 15.4 arcsec. The

---

[2]http://cxc.harvard.edu/ciao/

[3]http://cxc.harvard.edu/caldb/

[4]http://cxc.harvard.edu/ciao/threads/pointlike/

background region was centered around a nearby empty patch of sky that had no sources within a circle of radius 59.8 arcsec such that the area for the background region was ~ 15 times larger than the area for the source region. The source region was limited to only 15.4 arcsec because we wanted to maximize the extraction region yet there were other nearby sources that had to be avoided and not just masked out (see Figure 2).

Obs ID	Detector (With Filter)	Date (yyyy mm dd)	Off-axis Angle (arcmin)	Filtered Exposure Time (ks)	Counts (0.3 to 2.0 keV)	Background Fit Cash Statistic/dof
12238	ACIS-I VFAINT	2010 Sep 24	7.180	63.8	50	756/661
16028	ACIS-I FAINT	2014 May 16	5.950	65.1	49	168/148
16029	ACIS-I FAINT	2014 Nov 17	5.286	62.1	49	188/148
	EPIC-MOS1 Medium			42.9	79	437/537
0112800101	EPIC-MOS2 Medium	2001 Jan 2	5.448	42.3	67	436/536
	EPIC-PN Medium			35.6	175	525/540
	EPIC-MOS1 Medium			27.5	37	355/537
0112800201	EPIC-MOS2 Medium	2000 Dec 27	5.448	29.9	65	355/536
	EPIC-PN Medium			24.5	175	515/540
	EPIC-MOS1 Medium			35.0	57	437/537
0305860301	EPIC-MOS2 Medium	2005 Nov 25	5.812	35.0	67	435/536
	EPIC-PN Medium			33.0	200	536/540
	EPIC-MOS1 Medium			24.0	37	363/537
0305860401	EPIC-MOS2 Medium	2005 May 22	5.812	23.0	42	363/536
	EPIC-PN Medium			22.0	128	531/540
	EPIC-MOS1 Thin1			91.0	193	318/346
0791010101	EPIC-MOS2 Medium	2016 Dec 17	1.781	98.0	188	319/345
	EPIC-PN Medium			91.0	741	537/495
	EPIC-MOS1 Thin1			42.0	91	173/208
0791010301	EPIC-MOS2 Medium	2016 Dec 19	1.719	45.0	109	177/207
	EPIC-PN Medium			37.0	288	362/408
13515	ACS-WFC F606W	2014 Jun 30	1.138	2.4	...	...
	ACS-WFC F814W			2.5	...	...

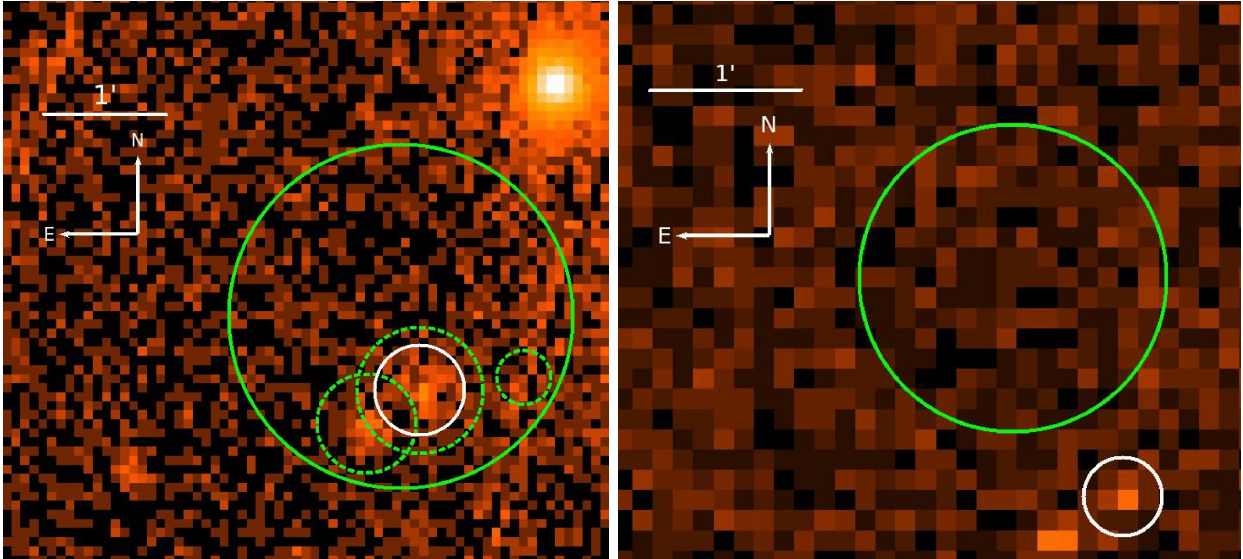Table 1:: Observational information of S26 in X-Ray and optical energy bands

Fig. 2.—:

Left: X-ray image of the PN detector for the *XMM-Newton* observation 0112800101 over the $0.2 - 3.0$ keV energy range. The large green circle has a radius of 82.7 arcsec, the green dotted circles have a radius of 23.9, 30.5, and 13.1 arcsec from left to right, and the white circle has a radius of 21.8 arcsec.

Right: X-ray image of the *Chandra* observation 12238 over the $0.2 - 3.0$ keV range. The green circle has a radius of 59.8 arcsec while the white circle has a radius of 15.4 arcsec.

Source extraction region is depicted as the white circle. Background extraction regions are depicted as the green circles with the dashed circles corresponding to regions that were masked from the background extraction region due to the sources within. The larger circle for the background extraction region was shifted for each observation and each detector for the *XMM-Newton* data in order to minimize the amount of the chip gap in the background region. For both of these images, we used a bin-size of 16 detector pixel, a min-max log scale, and a Gaussian smoothing of radius 3 in DS9.

Initially, we reprocessed the data from evt2 using the Ciao command `chandra_repro`[5]

---

[5]http://cxc.harvard.edu/ciao/ahelp/chandra_repro.html

using the default settings—observation 12238 had to be reprocessed with check_vf_pha set to true in order to properly reprocess the VFAINT data while the other two observation had check_vf_pha set to false. We then used the region files described above in `specextract`. The binning used for both the source and background files was the standard binning practice for `specextract`; namely, the data was grouped in such a way so each bin had a minimum of 15 counts.

2.2.2. *XMM-Newton Data*

We reduced the *XMM-Newton* data using SAS v15.0[6] and using the `xmmselect` command[7]. We have a total of six observations using the MOS1, MOS2, and PN detectors for each observation that totaled an effective exposure of 262.4 ks for MOS1, 273.2 ks for MOS2, and 243.1 ks for PN (see Table 1).

We created an image of the patch of sky that contained our source while applying filters and flags designed to remove artifacts. For the PN, MOS1, and MOS2 detectors, we selected the events with PATTERN in the $0 - 4$ range, set PI to be the preferred pulse height of the event with the range being between 200 and 3000 eV, and set 0xfa0000 to 0 to further clean up the images. We also used the standard practice of setting the #XMMEA_EP flag for the PN detector and #XMMEA_EM for the MOS1 and MOS2 detectors.

To filter time intervals with high background counts, we extracted light curves from the three detectors in each of the six observations over the $0.2 - 3.0$ keV energy range. The command `gtibuild` was used to create Good Time Intervals (GTIs) for each observation, which filtered out data that had any sharp peaks in the light curve. Then, `evselect` was

---

[6]http://xmmssc-www.star.le.ac.uk/SAS/

[7]https://heasarc.gsfc.nasa.gov/docs/xmm/abc/node9.html

used to filter the data based on the GTIs created with `gtibuild`. The sharp peaks in the light curves were removed in order to obtain the data that corresponded to the unflared time intervals which assists with our spectral fits that were taken.

We then extracted the spectra for our source and background by using the filtered event files via the `xmmselect` command. The `xmmselect` command would then create a PI file and a filtered image for both our source and the background regions.

The source region used was a circle centered on the SNR with a radius of 21.8 arcsec that was limited to this size due to nearby sources (see Figure 2). The background region was chosen near the SNR, avoiding other nearby sources, and any chip gaps. The area of the background region was the same for each observation and each detector and was ~ 11.4 times larger than the source region area.

After the source and background spectra were extracted, we created the associated RMF and ARF files using the `rmfgen` and `arfgen` commands. We then ran `grppha` to group the files together similar to the grouping for the *Chandra* data, which used `dmgroup`, but with these bins having a minimum of 1 count to eliminate any empty bins.

2.2.3. X-Ray Spectral Analysis

After the spectra were extracted, we fit them using XSPEC v.12.9.0n[8].

Following the technique of Garofali et al. (2017), we first fit both a sky and instrument background model to our background spectra. This consisted of a pair of absorbed thermal plasma components as the sky background for both the *XMM-Newton* and *Chandra* data.

The instrument background model was different for each of the detectors. For the

---

[8]https://heasarc.gsfc.nasa.gov/xanadu/xspec/

PN detector, we used a broad Gaussian at 0 keV and a broken power law, while for the MOS1 and MOS2 detectors we used a pair of broken power laws. For *Chandra*, we used a combination of power laws and Gaussians. For more information about the background model, see Garofali et al. (2017).

After we acquired the best-fit background model, we fit the data for the source including the background model components and setting the sky and instrument background parameters to the fitted values. We scaled the normalization of the background by the relative size of the source data region to the background data region. We also included `tbabs` and `pshock` components when fitting the source with a metal abundance of 0.5 relative to solar abundance (calculated using the metallicity gradient found from Gazak et al. (2015) and using a distance of 3.7 kpc between S26 and the center of NGC 300)—this metal abundance was accounted for in the `pshock` model component and not the `tbabs` component. The `tbabs` component modeled the interstellar absorption along the line of sight[9] assuming a minimum value equal to the Galactic N_H (foreground value of 3.0×10^{20} cm^{-2} from COLDEN[10]) and any addition to that value being due to the column density from NGC 300, while the `pshock` component modeled X-ray emission from a constant temperature plane-parallel shock plasma[11].

We fit the six *XMM-Newton* observations and the three *Chandra* observations simultaneously to maximize the amount of counts for the SNR and restricted the energy range to be between 0.3 and 2.0 keV—including any higher energy data would just add the background noise because there was no significant detection above 2.0 keV for S26. The only free parameters for the source model were the column density, temperature, and

[9]https://heasarc.gsfc.nasa.gov/xanadu/xspec/manual/node251.html

[10]http://cxc.harvard.edu/toolkit/colden.jsp

[11]https://heasarc.gsfc.nasa.gov/xanadu/xspec/manual/node206.html

normalizations. The normalization for the source data for each observation was initially free, but the column density and temperature were the same for each observation because we wanted to allow the fit to normalize each observation separately to improve the fit. We also attempted fitting with the normalizations the same for each observation, with the normalizations the same but changed the energy range to be between 0.3 and 5.0 keV, and with the normalizations the same but the temperatures allowed to vary from observation to observation and detector to detector. There was also a model that included a `powerlaw` component with the normalizations freed and a model that only consisted of `tbabs` and `powerlaw` components with the normalizations freed. All of these various fits utilized Cash statistics (see Cash (1979)).

2.3.   Radio Data

Radio observations of S26 from Pannuti et al. (2000) and Payne et al. (2004) using data from *VLA* and *ATCA* have revealed a counterpart to the optically detected SNR. The data was obtained on 1993 May 22 for the 6 cm wavelength data and on 1998 June 13 for the 20 cm wavelength data. The beam size was ≈ 4" at 6 cm (4885 MHz) and ≈ 6" at 20 cm (1465 MHz) with an rms sensitivity of 36 μJy at 6 cm and 60 μJy at 20 cm. S26 was detected at 20 cm, but a counterpart was not detected at 6 cm—Pannuti et al. (2000) and Payne et al. (2004) measured roughly the same value for the flux density of the counterpart at 20 cm (namely 0.22 mJy). From these measurements, both papers gave a value for the radio spectral index α (defined such that flux density $S_\nu \propto \nu^{-\alpha}$) to be $> 0.70 \pm 0.05$ (for the purpose of this paper we adopted a lower limit to α of 0.65 and just calculated the various physical parameters using this limit), which is consistent with synchrotron emission. The *VLA* and *ATCA* observations lacked the angular resolution to resolve clearly any spatial structure in the radio counterpart to S26. In Section 3.4, we discuss how this data was

utilized to calculate the minimum energy needed to drive synchrotron radiation and the minimum strength of the magnetic field.

3. Results

Using the data extracted over the various wavelengths, we are able to measure a variety of physical parameters. From the optical data taken with *HST*, we can constrain the size of the SNR's shock as well as the mass and age of the progenitor star. From the X-ray data taken with *Chandra* and *XMM-Newton*, we can fit the X-ray spectra with various models to measure the best-fit temperature of the SNR as well as the density of surrounding gas using the normalization factor. From the radio data, we can measure the minimum magnetic field strength as well as the minimum energy needed to drive synchrotron radiation. All of these measurements are described in detail below.

3.1. Size from HST Data

We positioned ellipses by eye to a color image of S26 to find the size of the SNR; the color image is shown in Figure 1. The ellipse most likely to correspond to the size of S26 followed the middle of the shell edge. The lower limit was set to the inner edge of the shell while the upper limit was set to the outer edge of the shell. The edge of the shell was determined by using the DS9 tool `Contours` and adjusting the contour level to find the inner, outer, and middle parts of the shell edge for our ellipses that were placed by eye (see Figure 3 for the middle part of the shell edge contour). The semimajor axis is 0.78 ± 0.10 arcsec and the semiminor axis is $0.69^{+0.14}_{-0.12}$ arcsec, corresponding to 7.5 ± 1.0 pc and $6.7^{+1.2}_{-1.4}$ pc, respectively. We also found that S26 has an eccentricity of 0.47.

We corroborated the ellipse method by also calculating the radii using the DS9 tool
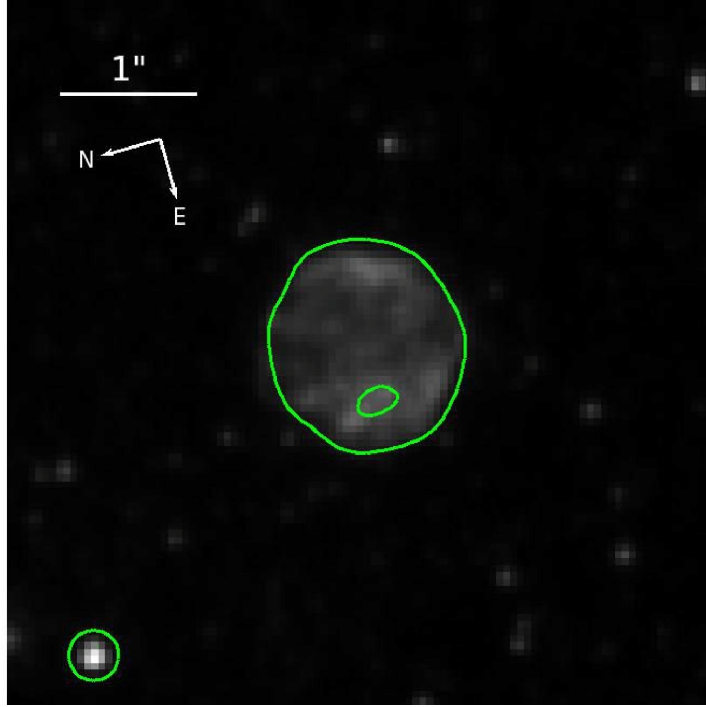
Fig. 3.—: Image of the F606W *HST* data with the contour used to determine the middle part of the shell edge (i.e. the best-fit value for the size of the SNR).

Projections aligned with the semimajor and semiminor axes (see Figure 1). This tool can be used to find the surface brightness function for the projected line. The semimajor and semiminor axes' brightness profiles give us a plot of the brightness versus distance that were used to find the semimajor and semiminor axes values—$0.79^{+0.19}_{-0.14}$ arcsec and $0.71^{+0.18}_{-0.24}$ arcsec, respectively. These values were found after performing third-order Taylor series expansions on the outer edges of the surface brightness functions. The values calculated are within the errors from the ellipse measurements.

Previously, the size was estimated to have a diameter of 33 pc using a distance assumption of 2.1 Mpc to NGC 300 (Blair & Long 1997). The *HST* data shows the SNR is a factor of ~ 2 times smaller, which is likely due to the improved spatial resolution—Blair & Long (1997) had a resolution of ~ 1" while the data from *HST* has a resolution of ~ 0.1".

3.2. Mass of the Progenitor

We use the well-established technique of fitting the CMD of the resolved stellar populations within 50 pc (5.2") of the SNR with stellar evolution models using the fitting package MATCH (Dolphin 2000, 2012, 2013) to constrain the age of the SNR progenitor (e.g., Badenes et al. 2009; Gogarten et al. 2009; Jennings et al. 2012; Williams et al. 2014a; Maund 2017). We begin by assuming that the progenitor of S26 was a massive star (> 7 $M_\odot$) that underwent core-collapse. In addition, we assume that nearby young stars were associated with the progenitor star. With these assumptions, we can use the ages of the nearby stars, as determined from their CMD to measure the most likely age (and inferred mass) of the progenitor.

To determine the ages of the nearby stars, we begin with a CMD of the sample of 1576 stars within 50 pc of the SNR center. These are shown with the red points in Figure 5. The grayscale in the plot shows the remaining $376,000$ stars in the field, which were scaled by area and used as a background sample for the fitting. The red plume of stars at WFC606W-WFC814W~ 1 is the red giant branch, and it is made up of old (> 500 Myr) stars. The blue plume at WFC606W-WFC814W~ 0 is the upper main sequence, and it consists of massive (> 3 $M_\odot$) young (< 500 Myr) stars. There are many more old stars than young ones, but the strong upper main sequence presence at this location in NGC 300 suggests that our assumption of a massive progenitor is reasonable. We then fit the CMD using the MATCH package (Dolphin 2012, 2013) to constrain the age distribution. While MATCH returns the ages up to 13 Gyr, we focus on the young component relevant to the SNR.

We show our results in Figure 4, where the population clearly shows a strong peak at an age of 8 Myr. We can use this age to infer the initial mass of the progenitor star assuming standard single star evolution. This age corresponds to the expected lifetime of a 25 $M_\odot$
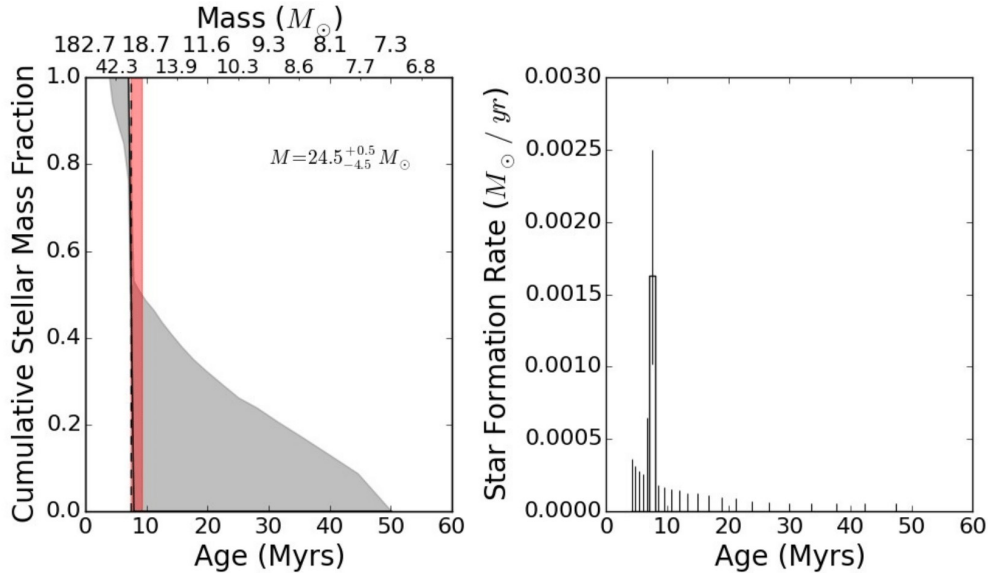
Fig. 4.—:

Left: Cumulative stellar mass fraction vs. age and mass used to constrain the age of the SNR progenitor star. The dashed vertical line marks the most likely age of the population surrounding the SNR, and the gray area shows the uncertainties on the cumulative fraction at each age. The red shaded region shows the median age of the population and the uncertainty.

Right: Star formation rate vs age from the fit, along with the uncertainties. A clear peak at 8 Myr is detected. This distribution results in the cumulative distribution and errors shown in left, where the fraction makes a rapid rise at 8 Myr ago.

star. The uncertainties of our age distribution, as determined from the MATCH `hybridmc` package (Dolphin 2012, 2013), are shown by the red shading in Figure 4, and correspond to 8 ± 1 Myr and 25^{+1}_{-5} M$_\odot$, assuming the Padova stellar evolution models (Marigo et al. 2008; Girardi et al. 2010). This, therefore, suggests that this is one of the most massive SNR progenitors found in the Local Volume. The CMD associated with this population as well as the differential extinction can also be seen in Figure 5 and they show that the result is not sensitive to the amount of differential extinction associated with this population.
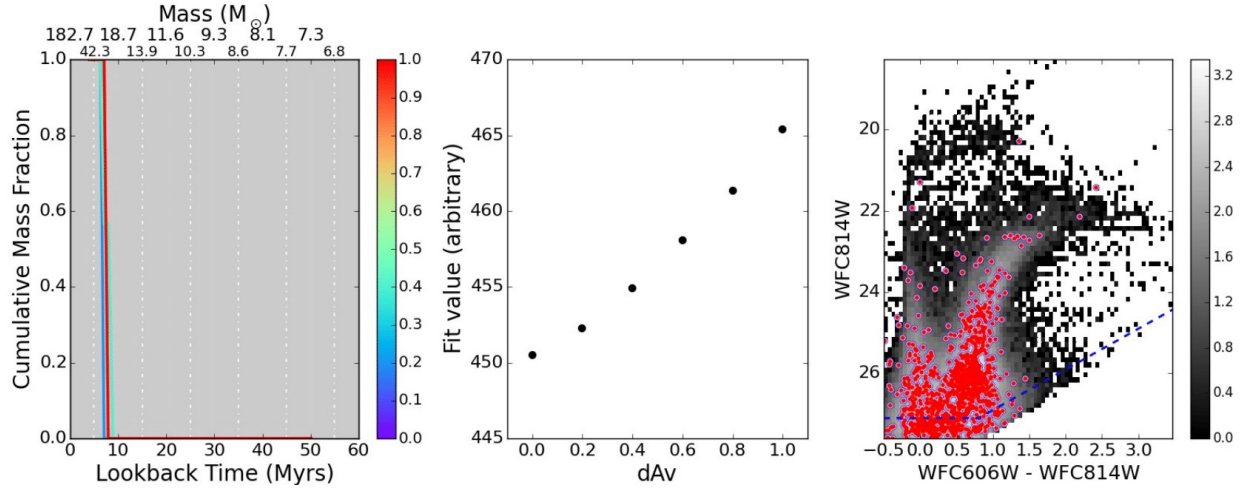
Fig. 5.—:

Left: Cumulative Stellar Mass Fraction versus age (Lookback Time) for several different assumed dAv values. The colors represent different fits, and the result appears insensitive to the choice of dAv.

Middle: Plot depicting the fit values (lower is a better fit) based on Poisson maximum likelihood values (Dolphin 2000, 2012, 2013) for each assumed dAv. The best-fit is for dAv= 0. This value was adopted, and the final result is shown in Figure 4

Right: Color Magnitude Diagram of the region around N300-S26 used to find the star formation history in Figure 4. The red points are the 1576 stars within 50 pc of the SNR center, and the grayscale shows the distribution of the remaining 376,000 stars in the field, which were scaled by area and applied as a background sample during the fitting. The dashed line shows the 50% completeness limit. The area above this line was included in the fit.

3.3. X-Ray Spectra

We simultaneously fit nine observations (total of 21 different data sets due to the various detectors) from *Chandra* and *XMM-Newton*; each of the effective exposure times can be found in Table 1. We found that our best joint fit to the extracted spectra had a hydrogen column density of $(9.7^{+6.4}_{-4.8}) \times 10^{20}$ cm^{-2} which is a slightly larger than the value for the foreground, 3.0×10^{20} cm^{-2}, obtained from COLDEN,[12], suggesting a small amount of extinction due to NGC 300 as well as possibly from S26.

For each data set, we first fit a model to the extracted background data and found the normalization values for the sky and instrument modeled backgrounds. Then, we fit all of the source data with the modeled background data. The background models were all frozen to the values determined from their individual fits.

We fit the source data to a model consisting of `tbabs` and `pshock` components using a distance of 2 Mpc and a metal abundance of 0.5 (calculated using the metallicity gradient found from Gazak et al. (2015) and using a distance of 3.7 kpc between S26 and the center of NGC 300). The fitted values can be found in Table 2 for having all of the normalizations tied together (see Figure 6 for the plotted spectra). The fit quality for the tied normalizations was excellent showing robust cross-calibration of the extractions. We also fit the spectra with the normalizations not tied together, the normalizations tied together and extending the energy range to be between 0.3 and 5.0 keV, and the normalizations tied together but the temperatures allowed to vary from observation to observation and detector to detector (see Table 3 for a breakdown of the varying temperatures), but found no significant change in the resulting parameter values (see Table 2). The values from the models in which normalizations were not tied together did result in significantly different parameters, but

---

[12]http://cxc.harvard.edu/toolkit/colden.jsp

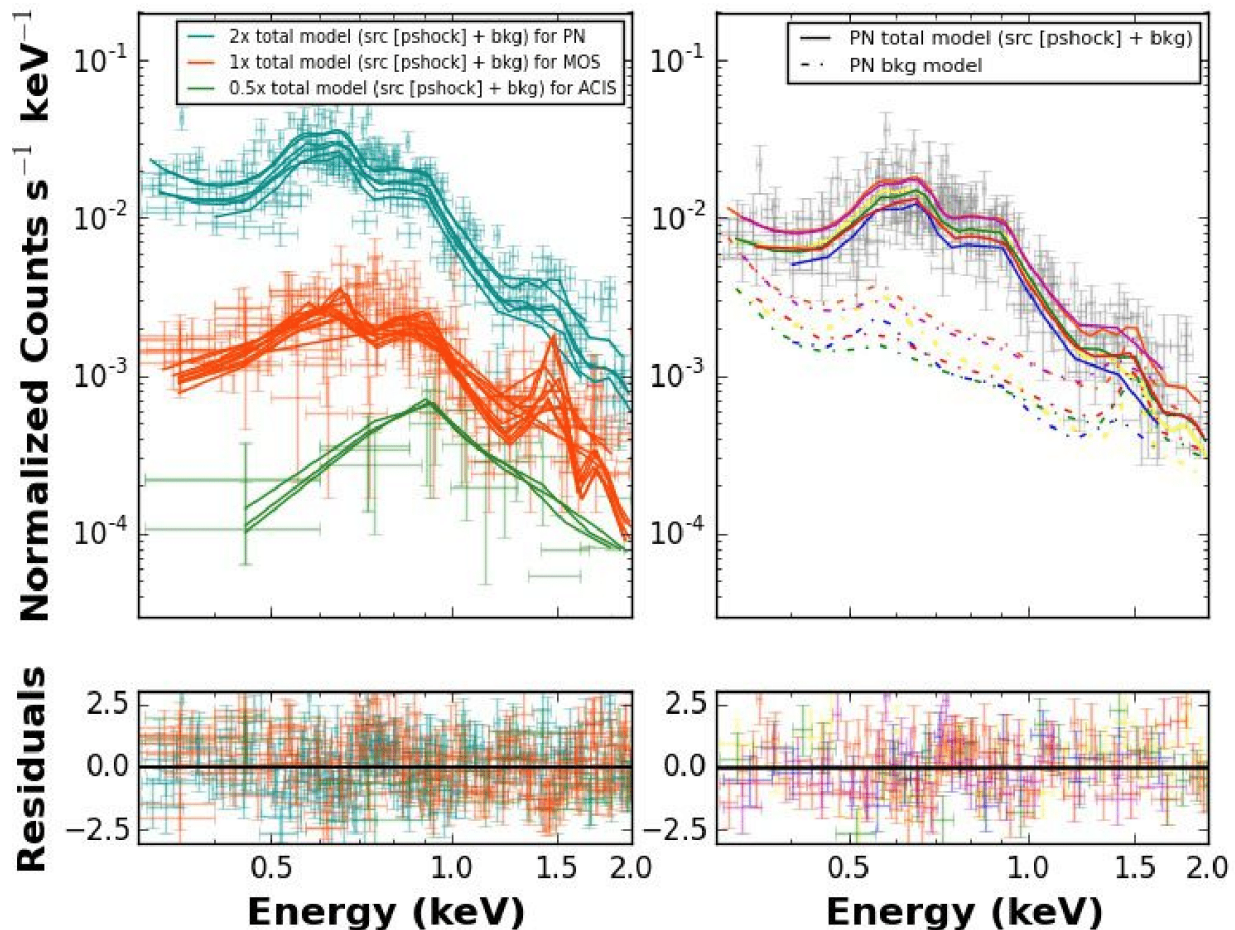the fit was not significantly better and the tied normalizations are more physically plausible.

Fig. 6.—: X-ray spectral fit using `tbabs*(pshock)` and having the normalizations tied. The right-hand graph is the PN data with the six observations (0112800101, 0112800201, 0305860301, 0305860401, 0791010101, and 0791010301) corresponding to blue, yellow, green, red, orange, and magenta, respectively.

The best-fit temperature was 0.77 ± 0.13 keV which is close to the typically measured temperature of 0.7 keV for nearby SNRs (Long et al. 2010b; Maggi et al. 2016). This temperature could be indicative of a pulsar heating up the surrounding gas or due to the SNR being young and expanding into a dense ambient medium. To test if there was a

Parameter	tbabs*(pshock) Normalizations Tied (90% Confidence)	tbabs*(pshock) Normalizations Free	tbabs*(pshock) Normalizations Tied $0.3-5.0$ keV
N_H (10^{22} cm^{-2})	$(9.7^{+6.4}_{-4.8}) \times 10^{-2}$	$(9.7 \pm 2.1) \times 10^{-2}$	0.11 ± 0.02
kT (keV)	0.77 ± 0.13	0.77 ± 0.06	0.73 ± 0.05
\<PShock Normalization\>[a]	$(5.4^{+2.0}_{-1.1}) \times 10^{-6}$	$(5.5 \pm 0.45) \times 10^{-6}$	$(5.7 \pm 1.1) \times 10^{-6}$
Photon Index	...	...	...
\<PowerLaw Normalization\>[b]	...	...	...
Cash Statistic/dof	7735/9025	7716/9005	15960/29915
\<Un-absorbed Luminosity\> (erg s^{-1})[d]	$\sim 6.3 \times 10^{36}$	...	...

Parameter	tbabs*(pshock) Normalizations Tied Temperature Free	tbabs*(pshock+powerlaw) Normalizations Free	tbabs*(powerlaw) Normalizations Free
N_H (10^{22} cm^{-2})	$(9.4 \pm 1.9) \times 10^{-2}$	0.30 ± 0.08	0.87 ± 0.07
kT (keV)	0.79 ± 0.04[c]	0.53 ± 0.09	...
\<PShock Normalization\>[a]	$(5.3 \pm 0.9) \times 10^{-6}$	$(9.3 \pm 2.4) \times 10^{-6}$	...
Photon Index	...	5.3 ± 0.6	8.4 ± 0.5
\<PowerLaw Normalization\>[b]	...	$(2.1 \pm 0.9) \times 10^{-6}$	$(2.2 \pm 0.2) \times 10^{-5}$
Cash Statistic/dof	7725/9005	7574/8983	7755/9005
\<Un-absorbed Luminosity\> (erg s^{-1})[d]	...	...	...

[a] Average normalization for pshock component of fit. For tied normalization fits, the average value is just the normalization value fitted. Defined as $(10^{-14}/(4\pi[D_A(1+z)]^2)) \int n_e n_H dV$ where D_A is the distance to the source in cm, z is the redshift, n_e is the electron number density in cm^{-3}, and n_H is the hydrogen number density in cm^{-3}.

[b] Average normalization for powerlaw component of fit. Defined as photons/keV/cm^2/s at 1 keV.

[c] Average temperature over the various observations and various detectors. For a more detailed view of the temperature values for the different observations and detectors for the tbabs*(pshock), normalizations tied, temperature free fit see Table 3.

[d] Average un-absorbed luminosity over the nine different observations (six *XMM-Newton* and three *Chandra*) between the $0.3-2.0$ keV energy range.

Table 2:: X-ray spectral fits to the source data based on various different fit parameters. Best-fit spectral fit corresponds to the tbabs*(pshock) with the normalizations tied. The standard practice for these fits are to list the 1σ uncertainties for the values and to have the energy levels be between $0.3-2.0$ keV. This is the practice used unless otherwise stated.

Obs ID	Detector (With Filter)	Date (yyyy mm dd)	kT (keV)
12238	ACIS-I VFAINT	2010 Sep 24	0.71 ± 0.15
16028	ACIS-I FAINT	2014 May 16	0.78 ± 0.13
16029	ACIS-I FAINT	2014 Nov 17	0.66 ± 0.11
	EPIC-MOS1 Medium		0.93 ± 0.21
0112800101	EPIC-MOS2 Medium	2001 Jan 2	0.80 ± 0.17
	EPIC-PN Medium		0.86 ± 0.14
	EPIC-MOS1 Medium		0.75 ± 0.22
0112800201	EPIC-MOS2 Medium	2000 Dec 27	0.85 ± 0.22
	EPIC-PN Medium		1.0 ± 0.2
	EPIC-MOS1 Medium		0.55 ± 0.11
0305860301	EPIC-MOS2 Medium	2005 Nov 25	0.86 ± 0.18
	EPIC-PN Medium		0.80 ± 0.12
	EPIC-MOS1 Medium		0.74 ± 0.22
0305860401	EPIC-MOS2 Medium	2005 May 22	0.90 ± 0.35
	EPIC-PN Medium		0.87 ± 0.17
	EPIC-MOS1 Thin1		0.68 ± 0.09
0791010101	EPIC-MOS2 Medium	2016 Dec 17	0.76 ± 0.11
	EPIC-PN Medium		0.76 ± 0.08
	EPIC-MOS1 Thin1		0.66 ± 0.12
0791010301	EPIC-MOS2 Medium	2016 Dec 19	0.85 ± 0.17
	EPIC-PN Medium		0.69 ± 0.10

Table 3:: The values for the temperature with 1σ uncertainties in the `tbabs*(pshock)`, normalizations tied, temperature free fit.

pulsar heating up the gas, we fit the source data to a model with `tbabs`, `pshock`, and `powerlaw` components. However, the results did not reveal any significant detection of a hard component to the spectrum (see Table 2). We also ran a fit that only had `tbabs` and `powerlaw` components, but also found no evidence of a hard component to the spectrum (see Table 2).

Previous observations of S26 also found a best-fit for the hydrogen column density and the temperature. Read et al. (1997) fit the data to a thermal Bremsstrahlung model and found the hydrogen column density to be $6.98^{+17.6}_{-3.2} \times 10^{20}$ cm^{-s} and the temperature to be $0.51^{+0.45}_{-0.29}$ keV. Both of our own best-fit values for the hydrogen column density and the temperature fall within the errors found by Read et al. (1997), which further supports our fits.

We also estimated a luminosity over the $0.3 - 2.0$ keV energy band using the XSPEC command `lumin` to be $\sim 3.9 \times 10^{36}$ erg s^{-1}, using a distance of 2 Mpc, and an unabsorbed luminosity of $\sim 6.3 \times 10^{36}$ erg s^{-1}.

The wings of the PSF of the nearest neighbor may result in a small amount of contamination in some of the extracted spectra (see Figure 2). In order to investigate the effects of such contamination, we ran a separate set of extractions where we masked any area within the 23.9 arcsec radius around this neighboring source. This alteration results in a significant loss of SNR counts, as the SNR light dominates in these locations; however, it is important to determine the maximum effects of the neighboring source.

We fit this masked out source region to a `tbabs*(pshock)` model and in order to better constrain this fit, we allowed the various normalizations from observation to observation and detector to detector to be varied individually since the relative amount of counts removed from each data set were too different from one another to justify the normalizations to be tied together. This model resulted in a hydrogen column density of $(7.0 \pm 2.0) \times 10^{20}$ cm^{-2},

a temperature of 0.75 ± 0.05 keV, an average normalization of $(4.4 \pm 11.3) \times 10^{-5}$ cm^{-5}, a luminosity of $\sim 3.5 \times 10^{37}$ erg s^{-1}, an unabsorbed luminosity of $\sim 5.1 \times 10^{37}$ erg s^{-1}, and a Cash Statistic/dof of 4855/4799 with these errors corresponding to the 1σ limit. These values are all within the errors derived for our fit to the full extraction area stated above, which suggests that the nearby source was not significantly affecting the fit.

As an additional check on our fitting, we also performed a very simple fit to only the PN detector data for observation 0791010101 since it had the most counts out of all of the observations and detectors and was one of the more on-axis observations that we had. For the total source extraction region and a `tbabs*(pshock)` model, the hydrogen column density was $(10 \pm 5) \times 10^{20}$ cm^{-2}, the temperature was 0.73 ± 0.11 keV, the normalization was $(5.5 \pm 2.2) \times 10^{-6}$ cm^{-5}, and the Cash Statistic/dof was 732/518. For the extraction region altered to remove any extended wings from the neighboring source and a `tbabs*(pshock)` model, the hydrogen column density was $(12 \pm 5) \times 10^{20}$ cm^{-2}, the temperature was 0.63 ± 0.10 keV, the normalization was $(4.3 \pm 1.8) \times 10^{-5}$ cm^{-5}, and the Cast Statistic/dof was 705/499. The temperatures and absorption parameters reported for each of these fits are equivalent within their uncertainties, and they are consistent with those for the full data set (see Table 2), again suggesting that the wings from the neighboring source are not strongly affecting the fits to the SNR spectrum.

3.4. Radio Properties of N300-S26

We used the previous observations by Pannuti et al. (2000) and Payne et al. (2004) and the newly found radius from *HST* to evaluate the integrated radio flux density of the SNR (from this we infer the total radio luminosity, L), the minimum total energy, $E_{\min}$, corresponding to the energy stored within the SNR in the form of relativistic particles, and the corresponding minimum magnetic field, $B_{\min}$.

Following Pacholczyk (1970), where equipartition is assumed (magnetic energy is equal to the total particle energy), the radio flux density, S_ν, may be expressed in the form of a power law as a function of frequency as

$$S_\nu = \beta \nu^{-\alpha} \tag{1}$$

where β is a constant. From this definition, the integrated flux density, S, over the frequency range ν_1 to ν_2 is

$$S = \int_{\nu_1}^{\nu_2} S_\nu d\nu \tag{2}$$

where ν_1 and ν_2 are 10^8 Hz and 10^{11} Hz, respectively. The integrated radio luminosity, L, of S26 is

$$L = 4\pi d^2 S = 4\pi d^2 \int_{10^8\ Hz}^{10^{11}\ Hz} \beta \nu^{-\alpha}\ d\nu, \tag{3}$$

where d is the distance to the SNR.

The measured flux density at 1.448 GHz and the radio spectral index for S26 was 0.22 mJy and a lower limit to α of 0.65, respectively (Pannuti et al. 2000; Payne et al. 2004). This results in a value for β of 1.9×10^{-21} erg cm^{-2} s^{-1} Hz$^{-1/4}$ for the values of α and flux density stated. Using these values and our adopted distance to NGC 300, we calculate a lower limit for the radio luminosity L of $\sim 1.7 \times 10^{34}$ erg s^{-1} over the frequency range between 10^8 Hz and 10^{11} Hz.

Next, we calculate the upper limit values for both $B_{\min}$ and $E_{\min}$ following Pacholczyk (1970):

$$
\begin{aligned}
B_{\min} &= (4/5)^{5/7} c_{12}^{2/7} (1+\xi)^{2/7} f^{-2/7} r^{-6/7} L^{2/7} \\
E_{\min} &= c_{13} (1+\xi)^{4/7} f^{3/7} r^{9/7} L^{4/7}
\end{aligned}
$$

where ξ is the ratio of the energies of the high mass ions and the relativistic electrons within the SNR (we assume a value of 40, which is consistent with measured values for this ratio

at the top of the Earth's atmosphere), f is a filling factor corresponding to the volume of the SNR that is filled by the magnetic fields and relativistic particles (we assume a value of 0.25 that is consistent with values for an SNR in the Sedov stage of evolution; Duric (1995); Pannuti (2000)), and r is the radius of S26 (an mean value of 7.05 pc from our measured ellipse). Finally, the upper limits for c_{12} and c_{13} are

$$c_{12} = \left(\frac{c_1^{1/2}}{c_2}\right)\left(\frac{2\alpha-2}{2\alpha-1}\right)\left(\frac{\nu_1^{\frac{1-2\alpha}{2}} - \nu_2^{\frac{1-2\alpha}{2}}}{\nu_1^{1-\alpha} - \nu_2^{1-\alpha}}\right)$$

$$c_{13} = 0.921 c_{12}^{4/7}$$

and in turn c_1 and c_2 are

$$c_1 = \frac{3e}{4\pi m_e^3 c^5} = 6.27\times 10^{18}$$

$$c_2 = \frac{2e^4}{3m_e^4 c^7} = 2.37\times 10^{-3}$$

where e is the charge of the electron, m_e is the mass of the electron, and c is the speed of light in a vacuum; therefore, c_1 has units of statCoulomb s^5 g^{-3} cm^{-5} and c_2 has units of statCoulomb^4 s^7 g^{-4} cm^{-7}. These equations yield values of 0.067 mG and 1.5×10^{49} erg for the maximum values of $B_{\min}$ and $E_{\min}$, respectively.

To obtain context for the measured values for L, B_{min}, and E_{min} for S26, we examined published values for these properties for Galactic and extragalactic SNRs (Duric 1995; Pannuti 2000; Lacey & Duric 2001; Reynolds 2012). We also computed the values for these properties for a sample of 23 Galactic SNRs from Green (2017)[13]. To generate this sample, we chose SNRs with clear shell-like radio morphologies, which also had robust measurements of spectral indices, flux densities at 1 GHz, angular extents, and distances. Known historical

---

[13]See http://www.mrao.cam.ac.uk/surveys/snrs/

SNRs like Cassiopeia A and SN 1006, which may still be in the free-expansion stage of evolution rather than the Sedov stage, were excluded from our study. For our sample, the median values of L, B_{min}, and E_{min} were 8.30×10^{33} erg s^{-1}, 0.027 mG, and 3.35×10^{49} erg, respectively; the standard deviations of the values for L, B_{min}, and E_{min} were 5.48×10^{34} erg s^{-1}, 0.028 mG, and 6.69×10^{49} erg, respectively.

Our computed values for L and E_{min} for S26 are both within one standard deviation of the computed median values for our sample of Galactic SNRs. Furthermore, they are both an order of magnitude less than the computed range of values for these parameters presented by Lacey & Duric (2001) for the sample of candidate radio SNRs in the galaxy NGC 6946. This discrepancy may be explained in part by the limiting sensitivity attained by the survey conducted by Lacey & Duric (2001), which could not detect candidate radio SNRs as faint as S26 at the distance of NGC 6946 (5.9 Mpc; Karachentsev et al. (2000)). In addition, the elevated star formation rate of NGC 6946 relative to NGC 300 produces indirectly a significant population of luminous resident candidate radio SNRs with proportionally higher values of L and E_{min}. The radio luminosity of S26 is also fainter than the calculated radio luminosities for candidate radio SNRs in M33 by Duric (1995) who assumed a distance of 840 kpc to that galaxy.

Regarding B_{min}, while our computed value for this property falls within the range of measured values for Galactic SNRs from Reynolds (2012) it is more than one standard deviation greater than the median value for B_{min} for the Galactic SNRs in our sample. It is also an order of magnitude less than the computed range of values computed by Lacey & Duric (2001) for the candidate radio SNRs in NGC 6946. We attribute the difference between our computed value for S26's B_{min} to the computed values for B_{min} by Lacey & Duric (2001) to limiting sensitivity of the radio observations analyzed in that work (similar to the cases of the discrepancies with computed values of L and E_{min}) but we cannot readily

explain why the value of B_{min} is significantly greater than the median value found for our sample of Galactic SNRs. New radio observations of S26 with enhanced sensitivity that can more clearly determine its spectral index of this source may help address this question.

4. Discussion

The temperature from our X-ray spectral fits and the radius of the source from *HST* allow us to estimate how long ago the supernova (SN) occurred. From Equation 2 of Hughes et al. (1998), this age is

$$t \ (yr) = 10^3 \left(\frac{kT}{1\text{keV}} \right)^{-1/2} \left(\frac{\theta_R}{10"} \right) \left(\frac{D}{50\text{kpc}} \right) \tag{4}$$

where kT is the temperature derived from the best-fit spectral model in keV, θ_R is the angular size in arcsec, and D is the distance to the source in kiloparsecs. We calculated that the SN associated with S26 occurred $(3.3^{+0.7}_{-0.6}) \times 10^3$ yr ago for S26.

We also calculate the electron number density, n_e, and hydrogen number density, n_H, from the normalization found in the spectral fits. Using

$$normalization = \frac{10^{-14}}{4\pi[D_A(1+z)]^2} \int n_e n_H dV \tag{5}$$

where D_A is the distance to the source in centimeters and z is the redshift—6×10^{24} cm and 4×10^{-4}, respectively. We assume that $n_e = 1.2 n_H$ and that n_H is constant throughout the SNR and has units of cm^{-3}. The $\int dV$ is just the spherical volume of the SNR using a radius of 7.1 pc (the average radius from the semimajor and semiminor axis). The normalization of $(5.4 \pm 1.0) \times 10^{-6}$ cm^{-5} results in a n_H of $2.2^{+0.9}_{-0.6}$ cm^{-3} and a n_e of $2.6^{+1.1}_{-0.7}$ cm^{-3}, again consistent with our young age and high density hypothesis. It is worth noting that we have assumed a constant n_H for this SNR due to there not being enough counts to have a model with more than one hydrogen density value. There could very well be a variable n_H across

the SNR, but with our limited photon statistics, we were only able to simplify our model to derive a constant n_H value.

We also derive the corresponding pressure of the SNR using

$$P/k \ (K \ cm^{-3}) = 2n_e T \tag{6}$$

where n_e is the electron number density in cm^{-3} with a factor of 2 to represent the total number of particles, both electrons and protons, T is the temperature of the SNR in K, and k is Boltzmann's Constant. With the n_e derived above and the temperature associated with 0.77 ± 0.05 keV (error at 1σ level), which corresponds to $(8.9 \pm 0.5) \times 10^6$ K, results in a P/k value of $(4.7^{+2.3}_{-1.5}) \times 10^7$ K cm^{-3} which correspond to a pressure of $(6.5^{+3.2}_{-2.1}) \times 10^{-10}$ Pa. This value can help us compare S26 to other SNRs by looking at the pressure due to the shock wave of both of these SNe. It is worth noting that this is a rough approximation because the ideal gas law is not perfectly applicable for this SNR because the ionization timescale is of the order of 10^{11}, which is outside of collisional ionization equilibrium.

We have also calculated the amount of mass swept up by the SNR using

$$M_X = f m_H n_H V \tag{7}$$

where f is the volume filling factor of the X-ray emitting plasma (assumed to be 1 for simplicity), m_H is the mass of a hydrogen atom, n_H is the hydrogen number density calculated from the normalization above, and V is the volume of the SNR (the ellipse from optical emission is assumed to be edge on for simplicity). This resulted in a M_X of 82^{+100}_{-47} $M_\odot$. This value can help us compare S26 to other SNRs by looking at the amount of matter swept up by the shock wave of both of these SNe as they propagate through space.

In order to get an estimate on the shock velocity of S26, we used conservation of energy and assumed that the deceleration of the material was constant after the second phase evolution of the SNR began (when 1 $M_\odot$ of matter was swept up). Doing so resulted in a

transition radius of $1.6^{+0.3}_{-0.1}$ pc using a density $\rho = m_H n_H = (3.7^{+1.5}_{-1.0}) \times 10^{-24}$ g cm^{-3} where m_H is the mass of hydrogen in g and n_H is the value derived above. We then assumed that the initial velocity at the beginning of the second phase was 3700 km s^{-1}, which was taken from Michael et al. (2003). This resulted in a shock velocity of 411^{+275}_{-122} km s^{-1} and an age for the SNR of $(2.6^{+0.7}_{-0.8}) \times 10^3$ yr. This age overlaps the age derived from Equation 4, which helps support this shock velocity.

To put S26 into context, we compare the values derived with Galactic SNRs. One such example of a Galactic SNR that has a similar temperature and size is G311.5–0.3, which was examined in detail in Pannuti et al. (2014, 2017). G311.5–0.3 is at a distance of 12.5 kpc, has a temperature of $0.68^{+0.20}_{-0.24}$ keV, and a radius of 9 pc; very similar to S26. Pannuti et al. (2014), derived many quantities from the X-ray spectral fit to G311.5–0.3—a shock velocity of 38.7 km s^{-1}, a remnant age of $(2.5 - 4.2) \times 10^4$ yr, a n_e of 0.20 cm^{-3}, a M_X of 21.4 $M_\odot$, a P/k ratio of 3.18×10^6 K cm^{-3}, and an unabsorbed luminosity of 4.09×10^{34} erg s^{-1}. It is worth noting that Pannuti et al. (2014) did not report any uncertainties for these values.

It is somewhat surprising that G311.5–0.3 has a similar size and temperature yet is so much older and has such a lower shock velocity than S26. Some of these differences between S26 and G311.5–0.3 are likely related to the vast difference in X-ray luminosity. This factor of 1000 in luminosity is consistent with a younger age and a denser medium. Naively, the ages of both of these SNRs should be similar if the remnant age is proportional to the radius and inversely proportional to the shock velocity ($v_s \sim \sqrt{kT}$). However, the shock velocity in S26 appears to be much higher leading to the large size at the relatively young age. Since both of these SNRs have similar radii and temperatures, one might expect that they would have similar ages. However, the age of S26 is an order of magnitude smaller. We note that the age for G311.5–0.3 is likely better constrained than for S26 because its

shock velocity was measured from CO observations by Andersen et al. (2011) and Hewitt et al. (2009); however, our measurements suggest very little chance that S26 is as old as G311.5–0.3, which is consistent with its much higher X-ray luminosity.

An explanation for the similar sizes and temperature despite very different ages could be attributable to the differences in the hydrogen number density. For S26, the n_H is approximately an order of magnitude larger than G311.5–0.3. This higher number density could result in a higher shock velocity in S26 explaining the younger age for the SNR. The higher number density in S26 also explains why the amount of mass swept up is significantly higher, as well as the fact that the number density results in the P/k ratio that is an order of magnitude higher for S26.

All of these differences support our hypothesis that the fitted temperature for S26 is due to this source being a young SNR that is expanding into a dense medium. It thus appears that the higher number density medium has played a large role in making S26 appear to be young even though the temperature and size are similar to G311.5–0.3.

5.   Conclusions

From multiwavelength observations of S26 using data from *Chandra*, *XMM-Newton*, *HST*, *VLA*, and *ATCA* we have constrained several of this SNR's physical properties. We have simultaneously fitted three different *Chandra* observations and six *XMM-Newton* observations to constrain the properties derived via X-ray observations as well as analyzing this SNR in the optical and radio wavelengths to get a more complete picture of this source.

We have measured a precise optical size for the SNR from *HST* which shows this SNR was much smaller than previous, ground-based measurements indicated—it has a semimajor axis of 7.5 ± 1.0 pc and semiminor axis of $6.7^{+1.2}_{-1.4}$ pc. From X-ray spectral fitting,

we estimated an unabsorbed luminosity, temperature, and intervening hydrogen column density—$\sim 6.3 \times 10^{36}$ erg s^{-1}, 0.77 ± 0.13 keV, and $(9.7^{+6.4}_{-4.8}) \times 10^{20}$ cm^{-2}, respectively. From radio observations, we measured the radio luminosity over the $10^8 - 10^{11}$ Hz frequency range and found the maximum values for B_{min} and E_{min} that are consistent with SNRs that had a high mass progenitor star—1.7×10^{34} erg s^{-1}, 0.067 mG, and 1.5×10^{49} erg, respectively. The age of the surrounding population of stars also suggests that the SNR had a relatively high mass progenitor—8 ± 1 Myr and 25^{+1}_{-5} M$_\odot$. Finally, we compared our extragalactic SNR to a similar Galactic SNR; namely, G311.5–0.3. S26 appears to be a younger and significantly more energetic SNR that is expanding into a denser medium than its Galactic analog—$(3.3^{+0.7}_{-0.6}) \times 10^3$ yr old and $2.2^{+0.9}_{-0.6}$ cm^{-3}.

REFERENCES

Andersen, M., Rho, J., Reach, W. T., Hewitt, J. W., & Bernard, J. P. 2011, ApJ, 742, 7

Badenes, C., Harris, J., Zaritsky, D., & Prieto, J. L. 2009, ApJ, 700, 727

Blair, W. P., & Long, K. S. 1997, ApJS, 108, 261

Blair, W. P., Winkler, P. F., & Long, K. S. 2012, ApJS, 203, 8

Bozzetto, L. M., Filipović, M. D., Vukotić, B., et al. 2017, ApJS, 230, 2

Carpano, S., Wilms, J., Schirmer, M., & Kendziorra, E. 2005, A&A, 443, 103

Cash, W. 1979, ApJ, 228, 939.

Dalcanton, J. J., Williams, B. F., Seth, A. C., et al. 2009, ApJS, 183, 67

Desai, K. M., Chu, Y.-H., Gruendl, R. A., et al. 2010, AJ, 140, 584

Dodorico, S., Dopita, M. A., & Benvenuti, P. 1980, A&AS, 40, 67

Dolphin, A. E. 2000, PASP, 112, 1383

—. 2012, ApJ, 751, 60

—. 2013, ApJ, 775, 76

Duric, N., Gordon, S. M., Goss, W. M., et al. 1995, ApJ, 445, 173.

Freedman, W. L., Madore, B. F., Hawley, S. L., et al. 1992, ApJ, 396, 80

Garofali, K., Williams, B. F., Plucinsky, P. P., et al. 2017, MNRAS, 472, 308

Gazak, J. Z., Kudritzki, R., Evans, C., et al. 2015, ApJ, 805, 182

Girardi, L., Williams, B. F., Gilbert, K. M., et al. 2010, ApJ, 724, 1030

Gogarten, S. M., Dalcanton, J. J., Williams, B. F., et al. 2009, ApJ, 691, 115

Green, D.A. 2017, 'A Catalogue of Galactic Supernova Remnants (2017 June Version)', Cavendish Laboratory, Cambridge, United Kingdom

Hewitt, J. W., Rho, J., Andersen, M., & Reach, W. T. 2009, ApJ, 694, 1266

Hughes, J. P., Hayashi, I., & Koyama, K. 1998, ApJ, 505, 732

Jennings, Z. G., Williams, B. F., Murphy, J. W., et al. 2012, ApJ, 761, 26

—. 2014, ApJ, 795, 170

Karachentsev, I. D., Sharina, M. E., & Huchtmeier, W. K. 2000, A&A, 362, 544.

Kong, A. K. H., Sjouwerman, L. O., Williams, B. F., Garcia, M. R., & Dickel, J. R. 2003, ApJ, 590, L21

Lacey, C. K., & Duric, N. 2001, ApJ, 560, 719.

Lee, J. H., & Lee, M. G. 2014a, ApJ, 786, 130

—. 2014b, ApJ, 793, 134

Long, K. S., Kuntz, K. D., Blair, W. P., et al. 2014, ApJS, 212, 21

—. 2010, ApJS, 187, 495

Maggi, P., Haberl, F., Kavanagh, P. J., et al. 2016, A&A, 585, A162

Marigo, P., Girardi, L., Bressan, A., et al. 2008, A&A, 482, 883

Maund, J. R. 2017, MNRAS, 469, 2202

Michael, E., McCray, R., Chevalier, R., et al. 2003, ApJ, 593, 809

Millar, W. C., White, G. L., Filipović, M. D., et al. 2011, Ap&SS, 332, 221

Pacholczyk, A. G. 1970, Series of Books in Astronomy and Astrophysics (San Francisco, CA: Freeman)

Pannuti, T. G. 2000, PhD thesis, University of New Mexico

Pannuti, T. G., Duric, N., Lacey, C. K., et al. 2000, ApJ, 544, 780

Pannuti, T. G., Filipović, M. D., Luken, K., et al. 2017, Serbian Astronomical Journal, 195, 23

Pannuti, T. G., Rho, J., Heinke, C. O., & Moffitt, W. P. 2014, AJ, 147, 55

Payne, J. L., Filipović, M. D., Pannuti, T. G., et al. 2004, A&A, 425, 443

Read, A. M., Ponman, T. J., & Strickland, D. K. 1997, MNRAS, 286, 626

Reynolds, S. P., Gaensler, B. M., & Bocchino, F. 2012, Space Sci. Rev., 166, 231.

Rodríguez, M. J., Baume, G., & Feinstein, C. 2016, A&A, 594, A34

Seok, J. Y., Koo, B.-C., & Onaka, T. 2013, ApJ, 779, 134

Williams, B. F., Peterson, S., Murphy, J., et al. 2014a, ApJ, 791, 105

Williams, B. F., Lang, D., Dalcanton, J. J., et al. 2014b, ApJS, 215, 9

Winkler, P. F., Blair, W. P., & Long, K. S. 2017, ApJ, 839, 83